Polarizing an antiferromagnet by optical engineering of the crystal field

A.S. Disa[1,2*], M. Fechner[1], T.F. Nova[1], B. Liu[1], M. Först[1], D. Prabhakaran[3], P.G. Radaelli[3], A. Cavalleri[1,2,3*]

[1]*Max Planck Institute for the Structure and Dynamics of Matter, Hamburg, Germany*

[2]*The Hamburg Centre for Ultrafast Imaging, Hamburg, Germany*

[3]*Clarendon Laboratory, Department of Physics, Oxford University, Oxford, UK*

Strain engineering is widely used to manipulate the electronic and magnetic properties of complex materials[1, 2]. An attractive route to control magnetism with strain is provided by the piezomagnetic effect, whereby the staggered spin structure of an antiferromagnet is decompensated by breaking the crystal field symmetry, which induces a ferrimagnetic polarization. Piezomagnetism is especially attractive because unlike magnetostriction it couples strain and magnetization at linear order[3], and allows for bi-directional control suitable for memory and spintronics applications[4, 5]. However, its use in functional devices has so far been hindered by the slow speed and large uniaxial strains required. Here, we show that the essential features of piezomagnetism can be reproduced with optical phonons alone, which can be driven by light to large amplitudes without changing the volume and hence beyond the elastic limits of the material. We exploit nonlinear, three-phonon mixing to induce the desired crystal field distortions in the antiferromagnet CoF_2. Through this effect, we generate a ferrimagnetic moment of 0.2 μ_B per unit cell, nearly three orders of magnitude larger than achieved with mechanical strain[6].

*corresponding authors

The control of magnetism via strain is most commonly based on magnetostriction. This effect relates an induced magnetization to the square of the applied stress and is restricted to systems with an equilibrium magnetization, like ferromagnets. Because the coupling is quadratic, the magnetic moment is only modulated in one direction when no external field is present.

Piezomagnetism, on the other hand, is a property of certain antiferromagnetic materials, which manifests as a linear coupling between an applied stress σ and an induced magnetization M of the form $M_i = \Lambda_{ijk}\sigma_{jk}$, where Λ is the piezomagnetic tensor [3, 7]. Hence, by exploiting the piezomagnetic effect, one can induce a magnetization of either sign from a crystal that possesses no net magnetization (see Fig. 1A).

CoF_2 is one of the simplest known piezomagnetic crystals. It has a rutile crystal structure with a body-centered cubic arrangement of cobalt ions, each surrounded by a fluorine octahedron with a tetragonal crystal field [8, 9]. Below T_N = 39K, it is a fully compensated type I antiferromagnet with easy-axis anisotropy, such that the magnetic moments on the Co ions at the center and corner of the cube point along the tetragonal *c* axis with opposite sign (magnetic space group $P4_2'/mnm'$, see Fig. 1A) [10, 11]. Piezomagnetism in CoF_2 arises from the site-selective modification of the Co crystal fields [6, 12]. Strain along the [110] direction distorts the crystal structure in such a way that the in-plane Co-F bond is shortened for the central sublattice and lengthened for the corner one (or vice-versa). As result, the relative energy splitting Δ of the Co t_{2g} orbitals is decreased on one site and increased on the other (Fig. 1B). In the d^7 configuration, the orbital magnetic moment scales as $m_L \sim \Delta^{-1}$; hence, the strain-induced distortion uncompensates the antiferromagnetically ordered moments and generates a net ferrimagnetic polarization. By changing the direction of the strain from tensile to compressive, the direction of the crystal field distortion reverses, and with that the sign of the induced magnetization.

The essential microscopic ingredient in the piezomagnetic effect is the antiparallel distortion of the Co-F bonds on each sublattice. Hence, it could also be induced also through the displacements of certain optical phonons alone, with the advantage of preserving the cell volume. New optical devices

enabling resonant driving of lattice vibrations at mid-infrared and terahertz frequencies open up the possibility to selectively control the structure of solids with light [13, 14, 15, 16]. At large phonon amplitudes, exploit lattice nonlinearities can be exploited to rectify atomic displacements and coherently mimic the effect of heteroepitaxial or externally applied strain [17, 18]. In particular, it was recently suggested that a rectification of the B_{2g} Raman phonon in CoF_2 would produce the same relative bond displacements as [110] uniaxial strain [19], at constant unit cell volume.

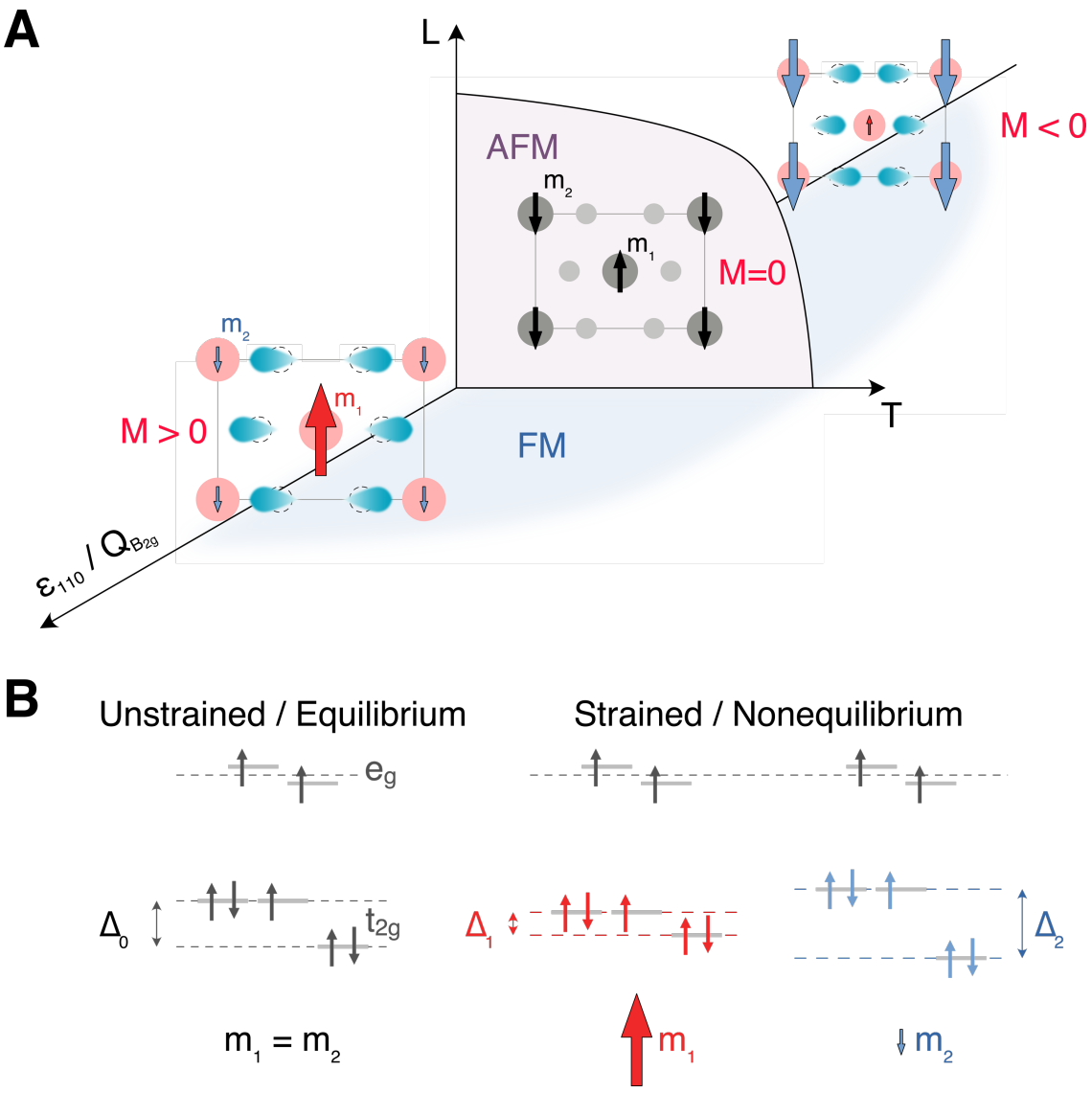

Figure 1. Piezomagnetic effect in CoF_2. (A) Under no strain, CoF_2 is antiferromagnetic below T_N. Under appropriate lattice deformation the antiferromagnetically aligned moments on the Co sites (m_1 and m_2) uncompensate, leading to ferrimagnetic order and non-zero magnetization (M). The lattice distortion (depicted in the ac plane) can be created by uniaxial strain along [110] (ε_{110}) or by atomic displacements along the B_{2g} Raman phonon ($Q_{B_{2g}}$). (B) The d electron crystal field levels for CoF_2 showing the origin of the piezomagnetic moment. The energy splitting between the t_{2g} levels (Δ) determines the orbital contribution to the magnetic moment ($\boldsymbol{m_L} \sim \Delta^{-1}$). In the undistorted structure, the energy splitting

between the t_{2g} levels (Δ) is the same for the two Co sites (left). When distorted, Δ shrinks for one site and grows for the other, hence changing the relative magnitudes of m_1 and m_2.

Here, we validate this approach and generate light-induced ferrimagnetic order in CoF_2 by using anharmonic coupling of three volume-preserving optical phonons to drive symmetry-breaking lattice distortions. In contrast to the case of applied strain, this *dynamical piezomagnetic effect* creates orders-of-magnitude larger displacements on time scales not limited by the speed of sound.

The desired lattice distortion corresponds to atomic motions along the coordinates of a Raman-active phonon of B_{2g} symmetry. Hence, it cannot be directly excited by light. Moreover, a purely impulsive excitation, typically achieved using near-infrared pulses, would produce an oscillating vibration about the equilibrium atomic positions and no net displacement of the lattice. Instead, we use the nonlinear coupling between resonantly driven infrared-active (IR) phonons and the Raman (R) mode, which can provide directional atomic motions away from equilibrium.

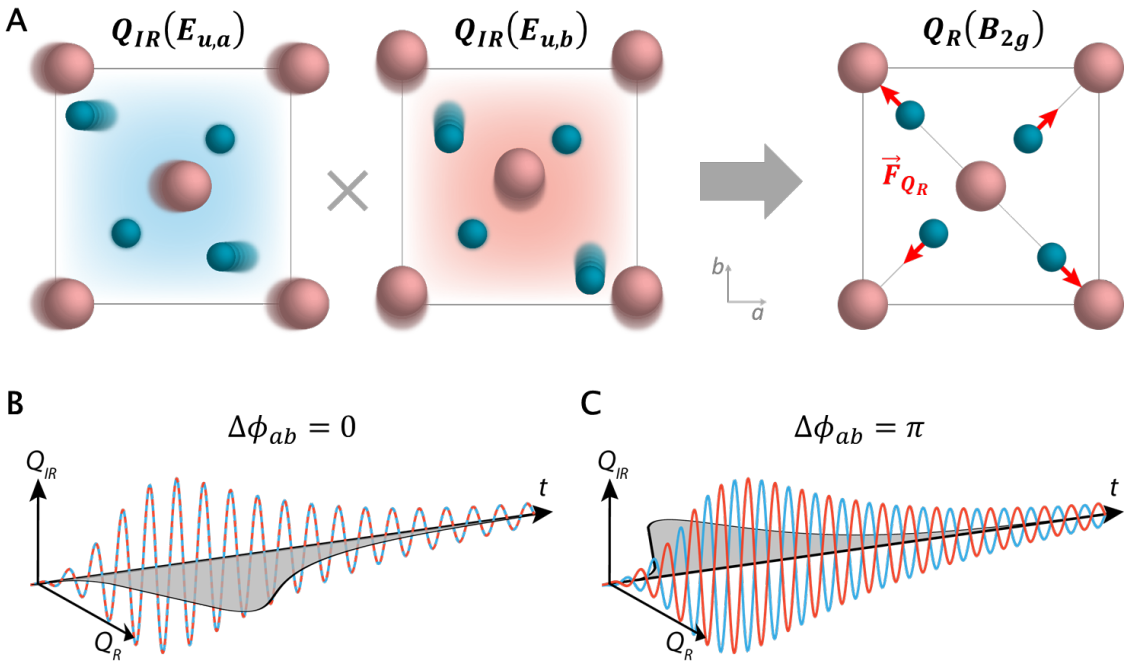

Figure 2. Breaking symmetry with phonons. (A) Two orthogonal, degenerate E_u phonons mix nonlinearly to displace the lattice along the B_{2g} Raman mode. The force on the lattice arising from the nonlinear interaction ($\vec{F}_{Q_R}$) is shown in red arrows. (B) The dynamics of the two IR modes (in red and blue) and the Raman mode (in grey) resulting from resonant excitation of both E_u modes by a terahertz pulse. The IR modes oscillate about their equilibrium positions, while the Raman mode is displaced away from equilibrium, creating a time-averaged structural distortion (solid shading). The two IR modes

in this case are pumped in phase ($\Delta\boldsymbol{\phi_{ab}} = \mathbf{0}$). (C) The phonon dynamics for the case when the two IR modes are driven out of phase ($\Delta\boldsymbol{\phi_{ab}} = \boldsymbol{\pi}$) showing that the Raman mode is displaced in the opposite direction.

Figure 2 describes the anharmonic lattice interaction used to drive the dynamical piezomagnetic effect [19]. The lowest order phonon coupling is given by the energy term $U = Q_{IR,1}Q_{IR,2}Q_R$, where Q_{IR} and Q_R denote IR and Raman mode coordinates. In the case that Q_R has B_{2g} symmetry, this coupling is symmetry allowed if $Q_{IR,1}$ and $Q_{IR,2}$ both have E_u symmetry. If the two modes are orthogonal and degenerate, this coupling provides a force onto Q_R that follows the envelope of the two optically driven IR modes, leading to a rectified displacement of the lattice along the B_{2g} mode direction (Fig. 2A). The time-averaged displacement of Q_R is proportional to the product of the two IR mode amplitudes, $\langle Q_R \rangle \propto |Q_{IR,a}||Q_{IR,b}| \cos\Delta\phi_{ab}$, where $\Delta\phi_{ab}$ is their relative phase of the two modes. Hence, the lattice displacement is maximal when the two IR modes are driven in phase, and the direction of the displacement flips when one of the two IR modes changes sign (*i.e.* $\Delta\phi_{ab} = \pi$), as shown in Fig. 2B,C. In CoF_2, the induced ferrimagnetic moment is linearly proportional to this $Q_R(B_{2g})$ displacement (see Supplement, Sec. S3).

Experimentally, in order to create the required lattice distortion and generate a net magnetization, one must simultaneously drive two degenerate, orthogonal IR modes with E_u symmetry. Figure 3A shows the optical conductivity along the *a* and *b* axes measured on the 100 µm thick CoF_2 crystal used in this experiment. The three conductivity peaks identify different E_u phonons with resonant frequencies close to 6, 8 and 12 THz. We resonantly and simultaneously drove the two IR modes at 12 THz (atomic motions also shown in Fig. 3A), for which the largest anharmonic coupling to the B_{2g} Raman mode was predicted (see Supplement, Sec. S3).

Intense THz excitation pulses were generated in a specially designed optical device that is based on two optical parametric amplifiers, a chirping stage, and a difference frequency generation stage using an organic crystal[20], as depicted in Fig. 3B. We produced 500 fs long pulses with peak electric fields up to ~10 MV/cm and a center frequency of ~12 THz (see Supplement, Sec. S1). To excite both *a* and

b axis modes simultaneously, the linearly polarized pump pulses were oriented at 45° with respect to the crystallographic axes (*i.e.* oriented along the [110] direction), impinging normally to the (001) face of the crystal. The sign of the induced Q_R displacement could then be flipped by rotating the pump polarization by 90° (along the $[1\bar{1}0]$). The induced magnetization was detected via complementary Faraday rotation and circular dichroism measurements at near-infrared/visible wavelengths.

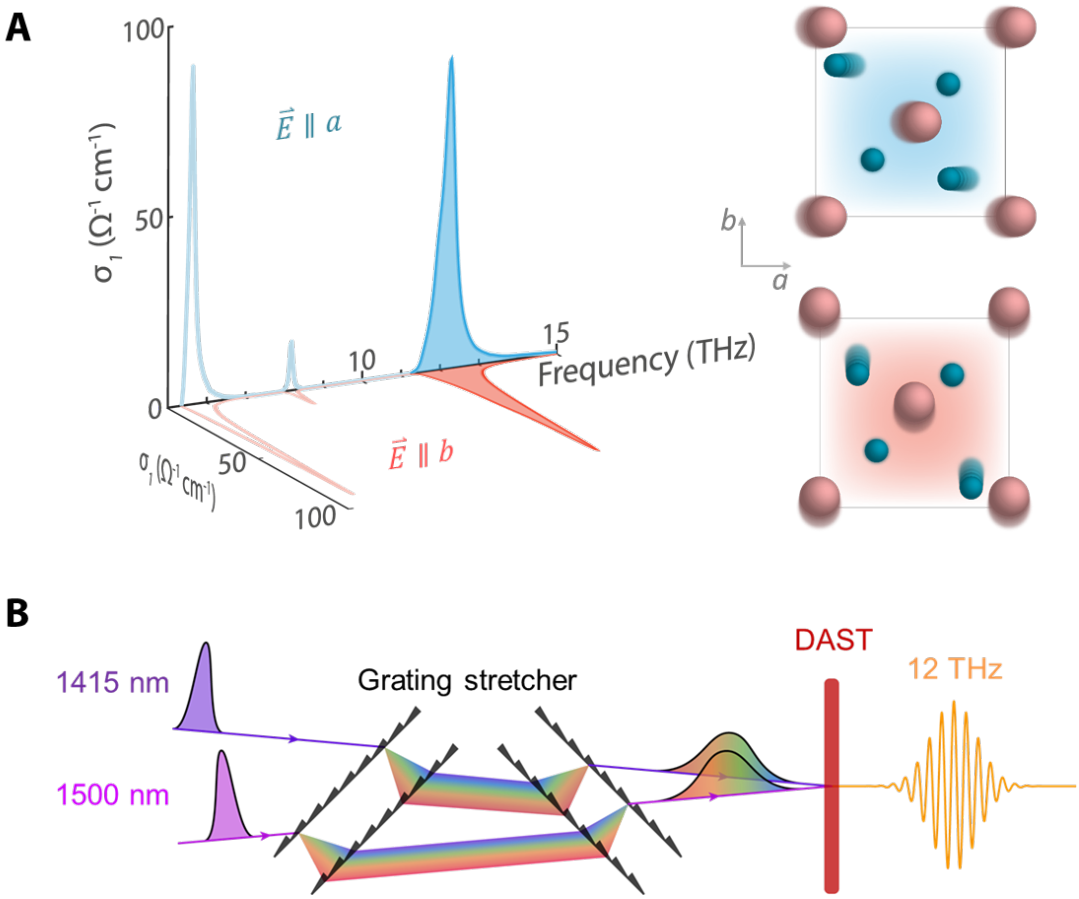

Figure 3. Driving degenerate infrared phonons in CoF_2. (A) Optical conductivity of CoF_2 at 6 K along the two orthogonal in-plane crystal axes (*a* and *b* in blue and red, respectively). The three peaks arise from the doubly degenerate (E_u) IR phonons. We pump the mode at 12 THz (solid shading). A top view of the atomic motions of the two components of the pumped mode is shown on the right. (B) Depiction of chirped pulse difference frequency generation for the pump pulses used in this experiment. Two near-IR pulses generated from co-seeded optical parametric amplifiers are stretched using two transmission grating pairs and combined non-collinearly on the organic crystal DAST (4-N,N-dimethylamino-4′-N′-methyl-stilbazolium tosylate) to produce narrow bandwidth, high-intensity pulses with a center frequency of 12 THz.

Time-resolved Faraday rotation measurements taken at T = 4 K are shown in Fig. 4A. Without the pump, no detectable rotation was observed. After photo-excitation, a pump-induced magnetization signal developed, which switched sign after ~7 ps and continued to grow in magnitude before reaching a maximum after ~200 ps. Rotating the pump polarization by 90°reversed the sign of the Faraday rotation, as expected by the anharmonic coupling mechanism discussed above. As a comparison, we conducted the same experiment on a ZnF_2 crystal, which has a nearly identical phonon spectrum to CoF_2, but is non-magnetic [21, 22]. The ZnF_2 crystal showed only a prompt polarization rotation (arising from pump-induced birefringence) and no long-lived signal, suggesting that the signal observed in CoF_2 is of magnetic origin.

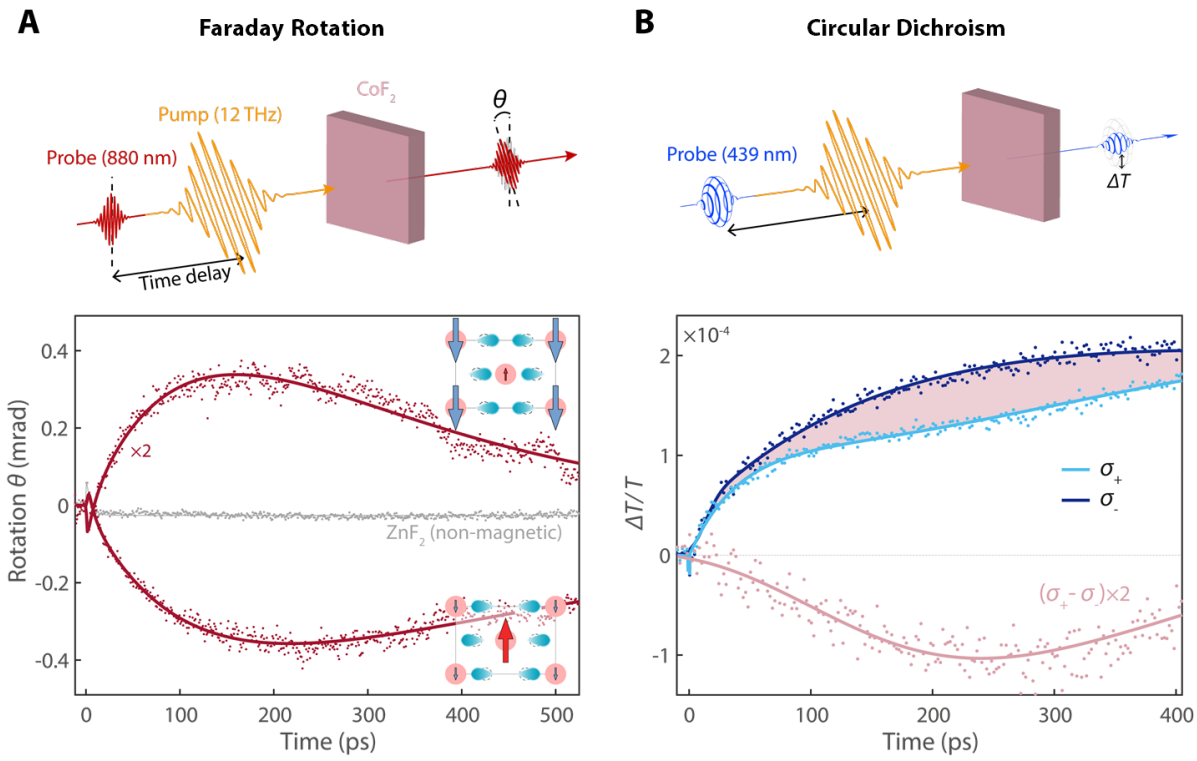

Figure 4. Time-resolved magneto-optical measurements. (A, top) Depiction of the THz pump-Faraday rotation probe measurement setup. The 12 THz pump was oriented at 45° with respect to the crystallographic *a* and *b* axes and the polarization rotation angle of a subsequent 880nm probe pulse was detected. (bottom) Faraday rotation data on CoF_2 (red) for two polarizations of the pump pulse (+45° and -45°) as a function of time delay. They display similar time dependences, with a small signal at short times that reverses, saturates and eventually decays back to zero. The inset shows the induced structural distortion (in the *ac* plane) and resulting ferrimagnetic state for the two pump polarizations. The same measurement taken on ZnF_2 is plotted in gray, exhibiting no long-lived response. (B, top) Depiction of the THz pump-circular dichroism probe measurement setup. The absorption of left and right circularly polarized probe pulses at 439 nm is detected as a function of time delay. (bottom) The relative change in transmission for left (dark blue) and right (light blue) circular polarized probe pulses. The shaded area depicts the circular dichroism, which is plotted on a 2× scale in pink. The

time dependence of the circular dichroism matches that of the Faraday rotation. In all panels, dots are measured data points and solid lines are double-exponential fits, as described in Supplementary Sec. SX.

In order to confirm the magnetic nature of the signal, we also carried out time-resolved circular dichroism measurements (Fig. 4B). At equilibrium, circular dichroism has been observed in CoF_2 near magnetically active electronic transitions in the presence of a large externally applied magnetic field, with the strongest effect found at the 439 nm absorption line[23, 24]. We probed the pump-induced change in transmission ($\Delta T/T$) at this wavelength using left and right circularly polarized pulses. A large difference in the relative $\Delta T/T$ was detected for the two polarizations after the THz pump excitation, with a time scale matching that of the Faraday rotation measurements.

Taken together, the observations reported above evidence a non-equilibrium state with a net magnetization and a response time of approximately 100 picoseconds.

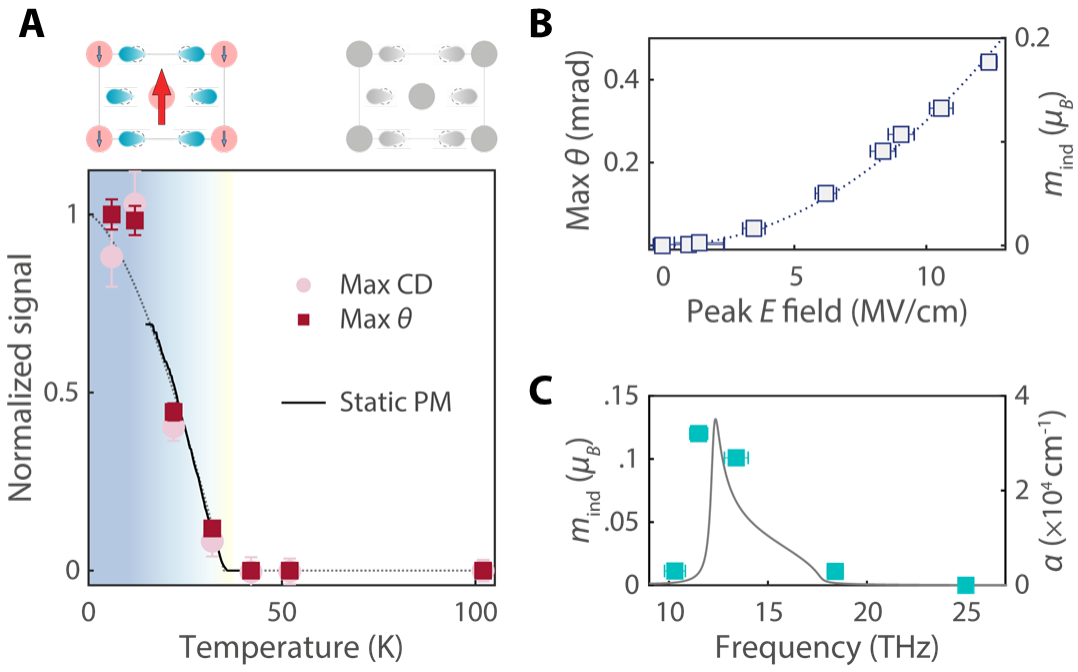

Figure 5. Characterization of the pump-induced state. (A) Temperature dependence of the maximum magnitude of the pump-induced Faraday rotation angle and circular dichroism (at ~200 ps), normalized to its value at 4 K. The static piezomagnetic response is shown in solid black (adapted from Ref. 25), and the dotted line is a guide to the eye. The insets at the top show the dynamical piezomagnetic state in the *ac* plane below T_N, and the distorted (but not magnetic) state above T_N. (B) Pump peak electric field dependence of the maximum Faraday rotation angle and the associated induced magnetic moment per unit cell at the sample surface. (C) Pump frequency dependence of induced moment per unit cell for a peak field of 10 MV/cm (solid squares) and extinction coefficient of the phonon (solid gray).

Figure 5A shows the magnitude of the pump-induced Faraday rotation and circular dichroism as a function of temperature. Both signals reduced upon warming the sample from 4 K and vanished above 40 K, coinciding with the Néel temperature T_N. The temperature evolution of the non-equilibrium magnetization followed that of the static piezomagnetic response of CoF_2 (Ref. 25). In both cases, the magnitude of the induced ferrimagnetic polarization should scale with the staggered magnetization of the equilibrium antiferromagnetic state.

The dependence of the Faraday rotation signal on the peak electric field of the pump pulse is shown in Fig. 5B. Using the Verdet constant for CoF_2 [26], we determined the induced magnetic moment at the sample surface m_{ind} and found that it scales as the square of the pump electric field (see Supplement, Sec. S2). Since the electric field linearly excites the two IR modes (Q_{IR}^{a} and Q_{IR}^{b}) and we expect $m_{ind} \propto Q_R$, this quadratic field dependence is consistent with the three-phonon coupling ($Q_{IR}^{a} Q_{IR}^{b} Q_R$) described in Fig. 3. Moreover, as a function of pump wavelength, the magnitude of the non-equilibrium moment showed a resonant enhancement at the eigenfrequency of the E_u phonon, as shown in Fig. 5C, demonstrating that the magnetization dynamics are indeed driven by the excited optical phonons.

We also found that at the maximum pump electric field of 12 MV/cm, the induced magnetic moment reached $m_{ind} \approx 0.2\ \mu_B$ per unit cell, in agreement with predictions from first-principles calculations (Fig. S4). This value is more than 400 times greater than the largest reported piezomagnetic moment induced statically in CoF_2 [6]. From the known piezomagnetic coefficients, a uniaxial stress of 40 GPa would be required to generate an equivalent moment, whereas typical tensile strengths of fluoride and oxide single crystals are < 0.5 GPa [27]. Since our pump excitation selectively distorted the $Q_{B_{2g}}$ mode without deforming the unit cell, much larger atomic displacements could be imposed than are possible with static strain (up to 2% of the equilibrium bond length; see Supplement, Sec. S3).

We now turn to a discussion of the dynamic behavior of the light-induced magnetization. A minimal model can be obtained from a free-energy description including the coupling between the antiferromagnetic order parameter (*L*), the induced magnetization (*M*), and the B_{2g} structural distortion (Q_R) (detailed in Supplement, Sec. S4). In this picture, the system initially occupies a minimum in the energy landscape where $M = 0$ and $L \neq 0$ (Fig. 6A). The magnetization dynamics are activated by the B_{2g} phonon displacement, which shifts the energy minimum to finite *M* and back on the time scale of the phonon lifetime (~5 ps). The subsequent evolution of the magnetic system after this prompt stimulus can be described as an overdamped oscillator: the kinetic energy imparted by the drive leads to the inertial growth of *M*, and at longer times the generated angular momentum equilibrates through spin-lattice relaxation processes [28, 29]. Figure 6B shows the computed $M(t)$ from this model for different values of the driving electric field, which reproduce well the experimental features.

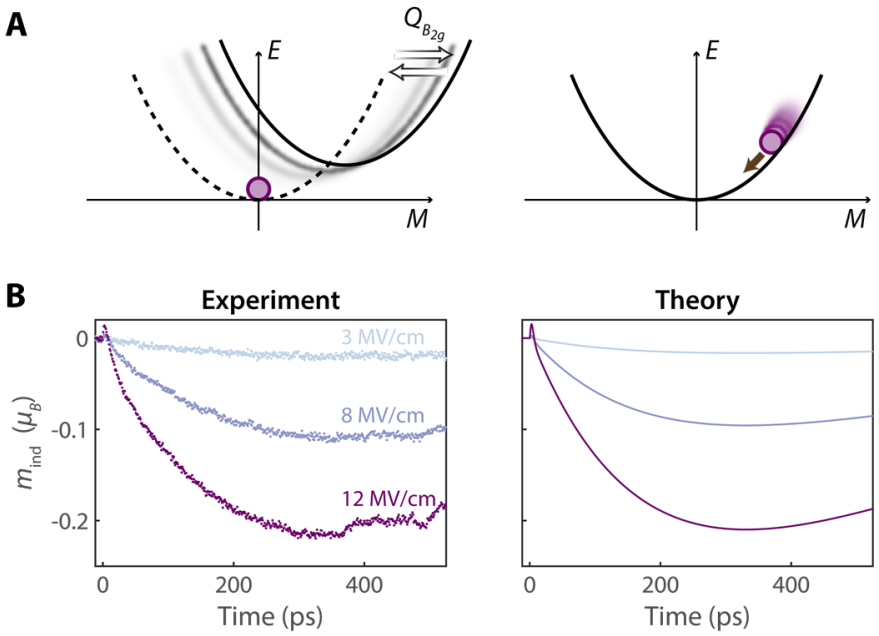

Figure 6. Pump-induced magnetization dynamics. (A,left) Illustration of the shift of the free-energy minimum to non-zero magnetization (*M*) upon displacing $Q_{B_{2g}}$, and (right) the subsequent evolution of the system in the equilibrium energy landscape. (B) Comparison between experiment and theory for the time dependence of the induced magnetic moment per unit cell for different pump electric field strengths. The theoretical calculations are obtained from the model described in Supplementary Sec. S4 and depicted in (A).

The proposed model provides an intuitive description of the experimentally observed magnetization dynamics. Microscopically, the dynamics of the magnetic moments of each sublattice are described by coupled Landau-Lifshitz-Bloch equations [30, 31]. In this framework, the observed growth and decay may arise from the slow longitudinal relaxation of M after the impulsive drive, with a time scale associated with the equilibration of the moments on the two sublattices. An outstanding question is the transfer mechanism between the prompt g-factor imbalance (created by the phonon) and the moment imbalance observed at later times (see Supplement, Sec. S4). One possibility is that the B_{2g} mode displacement modulates the anisotropy and exchange fields, which would split the magnon bands and could lead to the observed time-dependent behavior. Another possibility is that the transient lattice distortion is reinforced by the induced magnetization, creating a metastable state with slow dynamics, as has been observed in light-induced ferroelectrics [18].

The demonstrated phonon-driven, ultrafast analog of the piezomagnetic effect provides a new mechanism to manipulate magnetism in antiferromagnetic systems [32]. This dynamical effect circumvents typical limits of strain control, offering possibilities to explore novel, out-of-equilibrium phase behavior of correlated materials (like unconventional superconductors[1, 2]) and generate light-induced functional responses under extreme lattice deformations. Importantly, this approach differs from previous optical [33] and phononic [15, 16] methods of magnetic phase control, as it represents the rare case of a phase transition driven by coherent light-induced breaking of lattice symmetry.

Acknowledgments

We thank J. Chen for help preparing the samples and assistance with the optical experiment. This work received funding from the European Research Council under the European Union's Seventh Framework Programme (FP7/2007-2013)/ERC [grant agreement no. 319286 (QMAC)] and the Cluster of Excellence 'CUI: Advanced Imaging of Matter' of the Deutsche Forschungsgemeinschaft (DFG) - EXC 2056 - project ID 390715994. Work done at the University of Oxford was funded by EPSRC Grant No. EP/M020517/1, entitled Oxford Quantum Materials Platform Grant. A.S.D. was supported by a fellowship from the Alexander von Humboldt Foundation.

References

1. Chu JH, Kuo HH, Analytis JG, Fisher IR. Divergent Nematic Susceptibility in an Iron Arsenide Superconductor. *Science* 2012, **337**(6095)**:** 710-712.

2. Hicks CW, Brodsky DO, Yelland EA, Gibbs AS, Bruin JAN, Barber ME*, et al.* Strong Increase of T_c of Sr_2RuO_4 Under Both Tensile and Compressive Strain. *Science* 2014, **344**(6181)**:** 283-285.

3. Borovik-Romanov AS. Piezomagnetism, linear magnetostriction and magnetooptic effect. *Ferroelectrics* 1994, **162**(1)**:** 153-159.

4. Baltz V, Manchon A, Tsoi M, Moriyama T, Ono T, Tserkovnyak Y. Antiferromagnetic spintronics. *Reviews of Modern Physics* 2018, **90**(1)**:** 015005.

5. Liu Z, Feng Z, Yan H, Wang X, Zhou X, Qin P*, et al.* Antiferromagnetic Piezospintronics. *Advanced Electronic Materials* 2019, **5**(7)**:** 1900176.

6. Borovik-Romanov AS. Piezomagnetism in the antiferromagnetic fluorides of cobalt and manganese. *Sov Phys JETP* 1960, **11:** 786-793.

7. Dzialoshinskii IE. The problem of piezomagnetism. *Sov Phys JETP* 1958, **6**(3)**:** 621-622.

8. Oelkrug D. Absorption spectra and ligand field parameters of tetragonal 3*d*-transition metal fluorides. *Structutal and Bonding*, 1971, pp 1-26.

9. O'Toole NJ, Streltsov VA. Synchrotron X-ray analysis of the electron density in CoF_2 and ZnF_2. *Acta Crystallographica Section B Structural Science* 2001, **57**(2)**:** 128-135.

10. Stout JW, Matarrese LM. Magnetic Anisotropy of the Iron-Group Fluorides. *Reviews of Modern Physics* 1953, **25**(1)**:** 338-343.

11. Erickson RA. Neutron Diffraction Studies of Antiferromagnetism in Manganous Fluoride and Some Isomorphous Compounds. *Physical Review* 1953, **90**(5)**:** 779-785.

12. Moriya T. Piezomagnetism in CoF_2. *Journal of Physics and Chemistry of Solids* 1959, **11**(1-2)**:** 73-77.

13. von Hoegen A, Mankowsky R, Fechner M, Först M, Cavalleri A. Probing the interatomic potential of solids with strong-field nonlinear phononics. *Nature* 2018, **555**(7694)**:** 79-82.

14. Först M, Manzoni C, Kaiser S, Tomioka Y, Tokura Y, Merlin R*, et al.* Nonlinear phononics as an ultrafast route to lattice control. *Nature Physics* 2011, **7**(11)**:** 854-856.

15. Juraschek DM, Fechner M, Spaldin NA. Ultrafast Structure Switching through Nonlinear Phononics. *Physical Review Letters* 2017, **118**(5).

16. Nova TF, Cartella A, Cantaluppi A, Först M, Bossini D, Mikhaylovskiy RV*, et al.* An effective magnetic field from optically driven phonons. *Nature Physics* 2016, **13**(2)**:** 132-136.

17. Mankowsky R, Subedi A, Först M, Mariager SO, Chollet M, Lemke HT*, et al.* Nonlinear lattice dynamics as a basis for enhanced superconductivity in $YBa_2Cu_3O_{6.5}$. *Nature* 2014, **516**(7529)**:** 71-73.

18. Nova TF, Disa AS, Fechner M, Cavalleri A. Metastable ferroelectricity in optically strained $SrTiO_3$. *Science* 2019, **364**(6445)**:** 1075-1079.

19. Radaelli PG. Breaking symmetry with light: Ultrafast ferroelectricity and magnetism from three-phonon coupling. *Physical Review B* 2018, **97**(8).

20. Liu B, Bromberger H, Cartella A, Gebert T, Först M, Cavalleri A. Generation of narrowband, high-intensity, carrier-envelope phase-stable pulses tunable between 4 and 18 THz. *Optics Letters* 2016, **42**(1)**:** 129.

21. Balkanski M, Moch P, Parisot G. Infrared Lattice-Vibration Spectra in NiF_2, CoF_2, and FeF_2. *The Journal of Chemical Physics* 1966, **44**(3)**:** 940-944.

22. Giordano J, Benoit C. Infrared spectra of iron, zinc and magnesium fluorides: I. Analysis of results. *Journal of Physics C: Solid State Physics* 1988, **21**(14)**:** 2749-2770.

23. Wong YH, Scarpace FL, Pfeifer CD, Yen WM. Circular and magnetic circular dichroism of some simple antiferromagnetic fluorides. *Physical Review B* 1974, **9**(7)**:** 3086-3096.

24. Kharchenko N, Mil'ner A, Eremenko V, Bibik A. Magnetic circular dichroism in antiferromagnetic cobalt fluoride. *Zh Eksp Teor Fiz* 1988, **94:** 349.

25. Gaydamak TN, Zvyagina GA, Zhekov KR, Bilich IV, Desnenko VA, Kharchenko NF*, et al.* Acoustopiezomagnetism and the elastic moduli of CoF_2. *Low Temperature Physics* 2014, **40**(6)**:** 524-530.

26. Kharchenko NF. The linear magneto-optic effect as a manifestation of a higher order magnetoelectric effect. *Ferroelectrics* 1994, **162**(1)**:** 173-189.

27. Bolz RE. *CRC Handbook of Tables for Applied Engineering Science*, 2nd edn. CRC Press: Boca Raton, 1973.

28. Kimel AV, Ivanov BA, Pisarev RV, Usachev PA, Kirilyuk A, Rasing T. Inertia-driven spin switching in antiferromagnets. *Nature Physics* 2009, **5**(10)**:** 727-731.

29. Maehrlein SF, Radu I, Maldonado P, Paarmann A, Gensch M, Kalashnikova AM*, et al.* Dissecting spin-phonon equilibration in ferrimagnetic insulators by ultrafast lattice excitation. *Science Advances* 2018, **4**(7).

30. Atxitia U, Nieves P, Chubykalo-Fesenko O. Landau-Lifshitz-Bloch equation for ferrimagnetic materials. *Physical Review B* 2012, **86**(10)**:** 104414.

31. Atxitia U, Hinzke D, Nowak U. Fundamentals and applications of the Landau–Lifshitz–Bloch equation. *Journal of Physics D: Applied Physics* 2017, **50**(3)**:** 033003.

32. Song C, You Y, Chen X, Zhou X, Wang Y, Pan F. How to manipulate magnetic states of antiferromagnets. *Nanotechnology* 2018, **29**(11)**:** 112001.

33. Kirilyuk A, Kimel AV, Rasing T. Ultrafast optical manipulation of magnetic order. *Reviews of Modern Physics* 2010, **82**(3)**:** 2731-2784.